

Printed assemblies of GaAs photoelectrodes with decoupled optical and reactive interfaces for unassisted solar water splitting

Dongseok Kang¹, James L. Young², Haneol Lim¹, Walter E. Klein², Huandong Chen¹, Yuzhou Xi¹, Boju Gai¹, Todd G. Deutsch² and Jongseung Yoon^{1,3}*

Despite their excellent photophysical properties and record-high solar-to-hydrogen conversion efficiency, the high cost and limited stability of III-V compound semiconductors prohibit their practical application in solar-driven photoelectrochemical water splitting. Here we present a strategy for III-V photocatalysis that can circumvent these difficulties via printed assemblies of epitaxially grown compound semiconductors. A thin film stack of GaAs-based epitaxial materials is released from the growth wafer and printed onto a non-native transparent substrate to form an integrated photocatalytic electrode for solar hydrogen generation. The heterogeneously integrated electrode configuration together with specialized epitaxial design serve to decouple the material interfaces for illumination and electrocatalysis. Subsequently, this allows independent control and optimization of light absorption, carrier transport, charge transfer, and material stability. Using this approach, we construct a series-connected wireless tandem system of GaAs photoelectrodes and demonstrate 13.1% solar-to-hydrogen conversion efficiency of unassisted-mode water splitting.

n recent decades, technologies of photovoltaic energy conversion have made tremendous advancements in both efficiency and cost that could start to compete with fossil fuels^{1,2}. Although gigawatt scale solar plants are becoming a reality, converting such a large amount of energy into storable and transportable forms still remains an important challenge^{3,4}. In this context, solar-driven water splitting, mimicking photosynthesis in plants, is a promising approach that can potentially realize cost-effective hydrogen production by transforming sunlight into the energy stored in chemical bonds⁵⁻⁸. Among various materials systems considered, III-V compound semiconductors represent an excellent candidate for high-efficiency photocatalysis in solar fuel generation due to their highly favourable materials attributes, including near-ideal bandgap energy, appropriate band-edge alignment, as well as superior photophysical properties for the collection and transport of photogenerated carriers^{9–12}. Despite such compelling advantages, their practical application in solar water splitting has been limited primarily by the prohibitively high costs necessary to prepare device-quality single-crystalline materials¹³⁻¹⁵. Moreover, III-V compound semiconductors photocorrode spontaneously in highly acidic or alkaline electrolytes under the relevant electrochemical conditions of water splitting, leading to the rapid deterioration of intrinsic materials properties and associated electrode performance^{16,17}.

To address this challenge in materials stability, there have been extensive research efforts over the past decade on protective or passivation materials for silicon and III–V semiconductor photoelectrodes including transition metal oxides, metals, or metal silicides^{9,12,18–24}. Despite their success in providing enhanced stability and lifetime to various extents^{10,18,19,21}, most existing approaches are inherently limited due to the 'monofacial' electrode configuration. Such designs rely on a unified materials interface for both light

absorption and electrocatalysis, which often imposes demanding requirements for protective materials that must be optimized simultaneously for optical absorption, charge transport, catalysis, and corrosion resistance. Consequently, there is limited room for further improvement in terms of cost, performance, and stability of III–V electrodes based on existing wafer-based electrode designs.

Here, we present a strategy for III–V photocatalysis that can circumvent many of these limitations by exploiting printed assemblies of epitaxial III–V materials. In our approach, a thin film stack of GaAs-based epitaxial layers is released from the growth wafer by selective wet chemical etching of the sacrificial layer and printed onto a non-native transparent substrate to form an integrated photoelectrode system for solar-driven water splitting ^{25,26}. The resulting 'bifacial' GaAs photoelectrodes with a buried pn junction can effectively decouple materials interfaces for light absorption and electrocatalysis, affording greatly expanded flexibility in selecting the type and thickness of protective materials. We exploit this bifacial approach to fabricate series-connected tandem photocatalytic devices based on metal-passivated GaAs photoelectrodes and demonstrate unassisted-mode solar water splitting with solar-to-hydrogen conversion efficiency of 13.1%.

Fabrication of integrated bifacial GaAs photoelectrodes

Figure 1a schematically illustrates the fabrication procedures of integrated GaAs photoelectrodes for solar-driven photoelectrochemical (PEC) water splitting. As a photocatalytic semiconductor material, epitaxially grown stacks of $GaAs/Al_xGa_{1-x}As$ compound semiconductors originally designed for p-on-n type single-junction GaAs solar cells (Supplementary Fig. 1) were employed in conjunction with epitaxial lift-off and printing-based materials assemblies to enable an integrated bifacial electrode configuration

¹Department of Chemical Engineering and Materials Science, University of Southern California, Los Angeles, California 90089, USA. ²National Renewable Energy Laboratory, Golden, Colorado 80401, USA. ³Department of Electrical Engineering, University of Southern California, Los Angeles, California 90089, USA. *e-mail: js.yoon@usc.edu

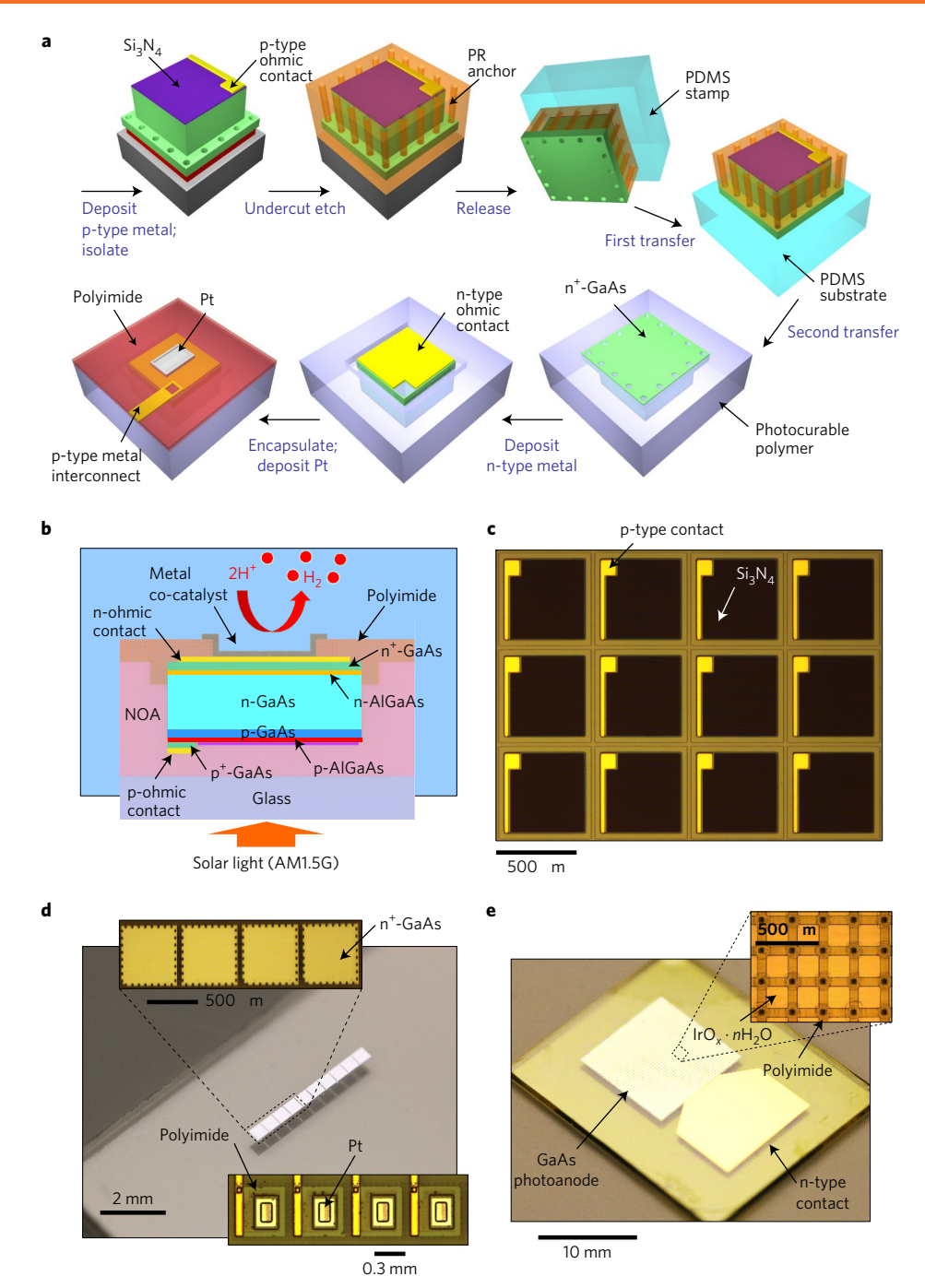


Figure 1 | Fabrication of integrated bifacial GaAs photoelectrodes. a, Schematic illustration of fabrication procedures for integrated GaAs photocathodes printed on a glass substrate for solar-driven photoelectrochemical water splitting. **b**, Cross-sectional illustration of an integrated GaAs photocathode fabricated by printing-based materials assemblies, where photocurable polymer (NOA; Norland Optical Adhesive) was used as a transparent printing medium. The structure is illuminated through the bottom of a glass substrate, while the electrolysis occurs on the other surface of the electrode immersed in an electrolyte. **c**, Optical microscope image of microscale GaAs photocathodes on the wafer after the formation of the p-type ohmic contact and ARC. **d**, Photograph of the exposed n⁺-GaAs after the printing on a glass substrate. The inset shows the catalytically active surface of the completed GaAs photocathodes after the PI encapsulation and deposition of Pt as a metal co-catalyst for the HER. **e**, Photograph of a centimetre-scale GaAs photoanode printed on a glass substrate. The inset shows a magnified view of the electrode surface.

with decoupled optical and reactive interfaces. Such procedures also allow the reuse of the growth wafer²⁷ or the growth of multilayer epitaxial assemblies²⁸, potentially providing a significant reduction of the materials cost¹⁵. We used 'bifacial' as a concise term to describe the approach where both front and rear surfaces of the photoelectrode are 'functional', in contrast to the wafer-based 'monofacial' photoelectrode that utilizes only the front surface. The fabrication process of GaAs photocathodes began with the

evaporation of metals (Pt/Ti/Pt/Au: 10 nm/40 nm/10 nm/80 nm) as a p-type ohmic contact followed by the removal of the p $^+$ -GaAs contact layer and the optional deposition of silicon nitride (Si $_3$ N $_4$, n=2.01 at 500 nm) on the exposed window layer (Al $_{0.40}$ Ga $_{0.60}$ As) as an anti-reflection coating (ARC) to reduce absorption and reflection losses, respectively. Active areas ($\sim\!495\times495\,\mu\text{m}^2$) of GaAs photocathodes were then delineated by photolithography and wet chemical etching in layouts that incorporate a two-level

Figure 2 | Photovoltaic and optical properties of epitaxial GaAs photocathodes on wafer and after transfer printing. **a**, Representative current density-voltage (J-V) curves of GaAs photocathodes on wafer as well as after transfer printing on a glass substrate at various materials configurations, including GaAs with an ARC (Si₃N₄, t = 80 nm) on wafer, GaAs with an ARC and Pt (t = 2 nm) on wafer, and GaAs without ARC after the printing on a glass substrate, measured under simulated AM1.5G solar illumination (1,000 W m⁻²). **b**, Measured (experimental; solid lines) near-normal incidence ($\theta \le 13^{\circ}$) reflectance spectra for the GaAs photocathodes in **a**. Computed reflectance spectra obtained from the FDTD calculation appear as dotted lines. **c**, Calculated absorption spectra of GaAs photocathodes on wafer in water, at varying thicknesses of continuous Pt film. The inset shows corresponding integrated solar flux absorption (S_abs), with the orange dashed line indicating the maximum S_abs of a printed GaAs electrode with an optimal ARC (S13N4, t = 71nm).

mesa structure such that etch holes for the etchant delivery to the sacrificial layer ($Al_{0.95}Ga_{0.05}As$) were made outside the junction area to minimize undesired materials degradation by the etchant. After selective removal of $Al_{0.95}Ga_{0.05}As$ by dilute hydrochloric acid^{29,30}, arrays of GaAs photocathodes were released from the growth wafer and assembled onto a glass substrate in a two-step transfer process mediated by a temporary polydimethylsiloxane (PDMS) substrate.

Through these printing steps, the bottom n+-GaAs contact layer was exposed to the front surface, forming the active electrode surface for catalysing water-splitting reactions. The top junction side of the device was oriented downwards, embedded in a photocurable printing medium (NOA 61) coated on a glass substrate. Subsequently, metals (AuGe/Ni/Au: 100 nm/30 nm/150 nm) for an n-type ohmic contact were deposited, followed by the exposure of the p-type metal contact through wet chemical etching and the formation of metal interconnects. Spin-coating and thermal curing of a thin (\sim 4 µm) layer of polyimide (PI) provided a liquid-proof encapsulation for the printed electrodes, except the central region $(100 \times 180 \,\mu\text{m}^2)$ left to be in direct contact with the electrolyte. Fabrication was completed by connecting external electrical lines to the electrode using flexible anisotropic conductive film (ACF, Elform) (Supplementary Fig. 2). More details of fabrication procedures are available in the Methods and Supplementary Methods. In this printed electrode configuration, sunlight illuminates through a glass substrate, while the hydrogen evolution reaction (HER) occurs on the opposite side of the immersed electrode, as schematically illustrated in Fig. 1b. Figure 1c shows optical micrographs of GaAs photocathodes on the growth wafer after forming the p-type ohmic contact and ARC. Figure 1d depicts photographic images of the photocathodes as printed on a glass substrate with an exposed n⁺-GaAs. The catalytically active surface after the encapsulation and the deposition of metal co-catalyst (Pt) also appears in the inset. Although the microscale electrode design was chosen here for the proof-of-concept demonstration, the reported materials and fabrication strategies can be equally applicable to conventional wafer-size electrode systems²⁸. Figure 1e shows photographic images of a centimetre-scale GaAs photoanode printed on a glass substrate, whose performance is close to that of microscale electrodes (Supplementary Figs 3 and 4).

Photovoltaic performance and optical properties

Efficient light management is one of key advantages that can be obtained from the integrated bifacial photoelectrode system. In particular, separating the materials interfaces for photon absorption and electrocatalysis via printed assemblies of epitaxial

Table 1 | Photovoltaic device characteristics of GaAs photocathodes.

	J _{sc} (mA cm ⁻²)	V _{oc} (V)	FF	η (%)
On wafer with ARC	21.4	0.938	0.731	14.6
On wafer with ARC, Pt (2 nm)	15.9	0.938	0.738	11.0
On glass	22.6	0.975	0.741	16.3

materials eliminates shadowing losses of the metal co-catalyst and therefore makes the absorbed photon flux substantially higher than conventional wafer-based electrode systems.

To quantitatively examine the light-absorbing capabilities of printed epitaxial GaAs photocathodes, baseline photovoltaic performance was evaluated under simulated AM 1.5G solar illumination (1,000 W m $^{-2}$). Figure 2a and Table 1 show the representative current density (*J*)-voltage (*V*) curves and extracted photovoltaic device characteristics of GaAs photocathodes, respectively, measured on wafer as well as after being transfer-printed on glass. The efficiency (η) and short-circuit current density (J_{sc}) were evaluated based on the measured active area (\sim 495 \times 495 \times 4m 2) at the light-absorbing interface, which includes the area shadowed by the metal contact. Due to the illumination overfilling the active electrode area, there is a small contribution of additional (\sim 10%) photon flux coupled into the device by the waveguiding effect of the glass substrate, which we have characterized using a set of apertures (Supplementary Fig. 5)^{31,32}.

For the electrodes measured on the wafer, 80-nm-thick Si₃N₄ was deposited as an ARC. For the printed devices, a simulated solar light was illuminated through the glass substrate to the emitter side of the GaAs electrodes to optimize both the light absorption and charge separation (Fig. 1b). The electron-beam deposition of 2-nm-thick Pt on ARC-coated GaAs photocathodes as a co-catalyst for the HER resulted in a noticeable decrease in J_{sc} from \sim 21.4 to \sim 15.9 mA cm⁻² owing to the attenuation and scattering of light in the metal layer. Such optical losses by the metal co-catalyst, albeit unavoidable in the conventional wafer-based system, are completely eliminated here in the bifacial electrode design, having a dedicated interface for light absorption. Moreover, the absorbed photon flux can be further improved by tailoring additional antireflective or diffractive layers in the isolated optical path. The $J_{\rm sc}$ of the GaAs photocathodes when printed on a glass substrate increased to \sim 22.6 mA cm⁻², in part due to the reduced reflection loss by the polymeric printing medium (that is, NOA) that served as an ARC.

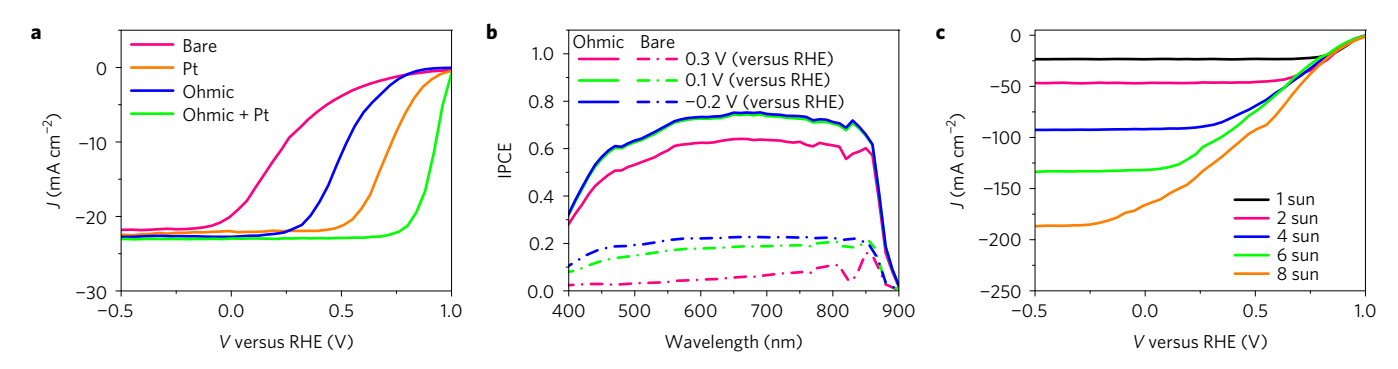


Figure 3 | Photoelectrochemical performance of integrated bifacial GaAs photocathodes in the HER. **a**, Representative current density-potential (*J-E*) curves of integrated GaAs photocathodes at various materials configurations, including bare GaAs, GaAs with Pt (*t* = 30 nm), GaAs with n-type ohmic metals (AuGe/Ni/Au), and GaAs with both an ohmic contact and Pt, where measurements were performed in an aqueous solution of sulfuric acid (0.5 M) under AM1.5G standard solar illumination using Pt wire and Ag/AgCl as counter and reference electrodes, respectively. **b**, Incident-photon-to-current efficiency (IPCE) for the GaAs photocathodes with ohmic metals (solid lines) and with bare GaAs (dash dotted lines) at various applied potentials of 0.3, 0.1, -0.2 V (versus RHE). **c**, *J-E* curves of GaAs photocathodes with an ohmic contact and Pt at various light intensities of simulated AM1.5G solar illumination.

The observed trends in photovoltaic performance were quantitatively consistent with the corresponding near-normal incidence $(\theta \le 13^\circ)$ reflectance spectra measured using a focused illumination source with an objective lens (Fig. 2b)^{33,34}. Notwithstanding their appreciable decrease in J_{sc} (Fig. 2a), the reflectance of ARC-coated GaAs electrodes on the growth wafer was only slightly (<absolute 5%) increased after the deposition of 2-nm-thick Pt, indicating that the attenuation by metals is the predominant cause of the observed optical loss. The measured reflectance spectra (solid line) showed good agreement with those (dotted line) calculated by the finite-difference time-domain (FDTD) method (Supplementary Figs 6 and 7). The small discrepancy in the case of printed electrodes (green) is attributed to the incomplete collection of the reflected light using an objective lens having a finite collection angle. Notably, the J_{sc} for the printed electrode is higher than that of GaAs with ARC due to the additional (~10%) photon flux from the aforementioned waveguide effect (Supplementary Fig. 5)³². To further estimate the absorption enhancement over conventional systems, absorption spectra of wafer-based GaAs photoelectrodes at varying nominal thicknesses (0 \sim 5 nm) of a Pt film were calculated by the FDTD method with a plane-wave light source illuminated from the air through the electrolyte (Fig. 2c and Supplementary Fig. 8). The inset to Fig. 2c shows the corresponding solar flux absorption (S_abs) weighted over the simulated AM1.5G standard solar illumination, given by the following equation,

$$S_{abs} = \frac{\int_{400 \text{ nm}}^{873 \text{ nm}} \frac{\lambda}{hc} A(\lambda) I_{1.5G}(\lambda) d\lambda}{\int_{400 \text{ nm}}^{873 \text{ nm}} \frac{\lambda}{hc} I_{1.5G}(\lambda) d\lambda}$$

where $h, c, A(\lambda)$ and $I_{1.5G}(\lambda)$ are Planck's constant, the speed of light, calculated absorbance and the standard solar irradiance (AM 1.5G; ASTM G-173), respectively³³. The S_abs of GaAs photoelectrodes decreased by \sim 0.11 and \sim 0.25 at Pt thicknesses of 2 and 5 nm, respectively, compared with that (\sim 0.78) of the electrode with no metals. On the other hand, the integrated absorption of the printed GaAs electrode with an optimal ARC (for example, Si_3N_4 , t=71 nm, Supplementary Fig. 9) is \sim 0.92, which corresponds to the \sim 76% enhancement over the wafer-based GaAs photoelectrode with 5-nm-thick Pt.

Photoelectrochemical performance in the HER

The photoelectrochemical (PEC) performance of integrated GaAs photocathodes towards the HER was studied using a potentiostat in a three-electrode configuration with an aqueous sulfuric acid (0.5 M $\rm H_2SO_4$) electrolyte under simulated AM1.5G solar illumination

(1,000 W m⁻²), where Pt and Ag/AgCl were used as counter and reference electrodes, respectively. During the measurements, the photoelectrodes were illuminated through their glass substrate, while the opposite was in contact with the electrolyte where the HER proceeded (Fig. 1b). Figure 3a shows current density (*J*)–potential (*E*) curves of the integrated GaAs photocathodes, obtained from a linear sweep voltammetry from -0.8 to $1.1\,\mathrm{V}$ (versus RHE) for various materials configurations implemented at the catalytic interface: bare GaAs, GaAs with Pt ($t=30\,\mathrm{nm}$), GaAs deposited with an n-type ohmic metal contact (AuGe/Ni/Au), and GaAs with both the n-type ohmic contact and Pt. The diagnostic maximum efficiency (η_{cathode}) of GaAs photocathodes for the HER was calculated by means of

$$\eta_{\text{cathode}}(\%) = \frac{J_{\text{max}} \times (E_{\text{max}} - E_{\text{H}^+/\text{H}_2}^{\circ})}{P_{\text{in}}} \times 100$$

where $J_{\rm max}$ and $E_{\rm max}$ are the current density and electrode potential at a maximum power point, $E_{\rm H^+/H_2}^{\circ}$ is the thermodynamic HER potential, and $P_{\rm in}$ is the power density of simulated AM1.5G solar illumination.

Distinct from conventional wafer-based systems, optically opaque layers of metals can be readily employed at the catalytic interface of bifacial electrodes to enhance both charge transfer and materials stability. Given that the buried, solid-state pn junction already provides band bending for separating the photogenerated carriers, introducing an ohmic metal contact at the electrode surface is highly beneficial to optimize the electron transfer from n⁺-GaAs layer to the metal co-catalyst by eliminating the energy barrier of upward band bending typical of n-type semiconductors in contact with electrolyte^{6,35}.

As summarized in Table 2, the GaAs photocathodes with an ohmic metal contact have a higher fill factor than the 'bare' GaAs electrode, which can be explained by more efficient charge transfer from the semiconductor to the electrolyte. The GaAs with Pt exhibited a higher onset potential and efficiency than GaAs with only an ohmic metal contact, indicating that the kinetic barrier inherent to the HER limits the performance of the latter electrodes. The best onset potential (1.022 V), fill factor (0.725) and efficiency (17.0%) were obtained when both an ohmic contact and Pt catalyst were deposited sequentially as a bilayer (that is, GaAs-ohmic-Pt), simultaneously enhancing carrier transport and catalytic activity.

To further elucidate the role of an ohmic metal contact in the photoelectrode performance, incident-photon-to-current efficiency (IPCE) spectra were measured at electrode potentials of 0.3, 0.1

Table 2 | Photoelectrochemical performance characteristics of integrated GaAs photocathodes in the HER.

	J _{sat} * (mA cm ⁻²)	$V_{ m onset}^{\dagger}$ (V)	FF	η _{cathode} (%)
Bare	21.8	0.936	0.134	2.5
Pt	22.5	1.004	0.509	11.2
Ohmic	22.8	0.834	0.372	7.1
Ohmic + Pt	23.1	1.022	0.725	17.0

^{*} J_{sat} (saturation current density) was determined at the voltage of $-0.5 \,\text{V}$ versus RHE. † V_{onset} (onset voltage) was decided at the current density of $-0.5 \,\text{mA}\,\text{cm}^{-2}$.

and -0.2 V (versus RHE) for bare GaAs and GaAs with an ohmic contact (Fig. 3b). For all wavelengths, the IPCE of GaAs with an ohmic metal contact is higher than that of bare GaAs because the energy barrier of upward band bending is eliminated to allow more efficient charge transfer, which is consistent with the trends in J-E performance (Fig. 3a) and electrochemical impedance spectroscopy (EIS) measurements (Supplementary Fig. 10).

(EIS) measurements (Supplementary Fig. 10).

As widely employed in photovoltaics 36,37, optical concentration is a straightforward route to improve the cost-effectiveness of III-V photocatalysis. In conventional electrode systems, however, increased illumination intensity accompanies the rigorous generation of gaseous products that scatter the light and therefore set the upper limit to the achievable optical concentration. The reported design of III-V electrodes with an isolated optical interface can couple with concentrated solar illumination using simple optical elements but also avoid the bubble-induced deterioration of electrode performance, thereby offering a practical means to significantly reduce the cost contribution of III-V materials. To this end, we characterized the performance of integrated GaAs photoelectrodes under illumination intensities greater than one sun. Figure 3c shows J-E curves of the GaAs photocathodes with an ohmic metal contact and Pt at various light intensities up to eight suns (\sim 8,000 W m⁻²). The J_{sc} increases linearly with the incident power of simulated solar illumination without any influence of generated bubbles, while the fill factor decreases because of the series resistance associated with the non-ideal spatial layout of metal contacts (Supplementary Table 1). Although beyond the scope of the present study, a fully optimized contact design could be readily accommodated in this integrated electrode configuration for concentrator solar fuel systems.

Surface passivation by optically thick metals

Flexible choices of materials and integration at the catalytic interface also allow unique pathways for protecting the semiconductor electrode from corrosive electrochemical conditions of water splitting. One of the critical requirements for protective materials of semiconductor photoelectrodes is facile transfer of photogenerated carriers (that is, electrons for photocathodes) from the semiconductor to the electrolyte. In this regard, metals naturally represent good candidate materials owing to their excellent electrical conductivity. However, poor optical transparency precludes their utility, at least in the optically thick regime, as protective materials for solar water-splitting systems. With the aid of the integrated bifacial electrode platform having decoupled optical and reactive interfaces presented here, we systematically examined the effectiveness of optically opaque layers of metals as protective coatings.

Figure 4a shows the time dependence of current density of GaAs photocathodes at an electrode potential of 0 V (versus RHE), where two different materials configurations such as bare GaAs and GaAs with an ohmic metal contact and Pt ($t=30\,\mathrm{nm}$) were compared in acidic electrolyte (0.5 M $\mathrm{H_2SO_4}$) for the HER. Notably, the metal-passivated GaAs photocathodes exhibited a remarkable stability for up to eight days, where the current density slightly decreased by $\sim 11\%$ over the entire period of

measurements (Supplementary Fig. 11). By contrast, the bare GaAs photocathodes with no protective coating degraded to producing a negligible cathodic current after only two days of continuous operation, highlighting the capacity for metal layers to protect the GaAs surface. The corresponding optical images (in the inset of Fig. 4a) depict nearly intact and severely degraded surfaces of metal-passivated and pristine electrodes, respectively. Exposed to the acidic electrolyte and cathodic conditions, the reductive decomposition of bare GaAs is inevitable ^{16,38}.

Based on these results, we postulate that metal layers in the passivated GaAs electrodes serve as a diffusion barrier that prevents protons in the electrolyte from reaching the GaAs surface and therefore delay the corrosion process (Fig. 4b). For such metal-passivated photocathodes, another important parameter influencing proton diffusion is the electrode potential, a thermodynamic driving force for electron transfer from the semiconductor to the electrolyte. With a high negative potential applied to the GaAs working electrode, more electrons are transferred to the electrolyte and participate in the HER, as evidenced by the increase of current density (Fig. 3a). Accordingly, more protons in the electrolyte are consumed in the HER, decreasing their near-surface concentration and prohibiting penetration into the metal layer, thus suppressing their capacity to reach and corrode the GaAs.

To examine the influence of electrode potential in this hypothesis, the stability of the GaAs photocathodes was tested under an applied bias (0 V versus RHE) and unbiased (that is, open-circuit) conditions as summarized in Fig. 4c. Throughout the testing, the electrode performance was periodically (every 6 h) assessed by measuring the photocurrent at 0 V (versus RHE). The stability of metal-passivated electrodes was substantially better when continuously biased, due to the increased levels of proton consumption and the correspondingly limited proton flux to the GaAs. By contrast, the electrode potential is less influential in the stability of unpassivated electrodes, because the surface of bare GaAs is already accessible to protons in the electrolyte. The comparatively shorter lifetime of metal-passivated electrodes than bare GaAs under the unbiased condition might be attributed to the accelerated oxidation of GaAs in the peripheral region of the metal by cathodically derived OH ions from the dissolved oxygen in the electrolyte³⁹.

To further confirm the role of metals as a barrier against proton diffusion, we tested the open-circuit stability of a set of metal-passivated electrodes with a range of metal thicknesses. Figure 4d shows the photocurrent density of GaAs photocathodes having a bilayer (Ti/Pt) metal coating with Ti thicknesses of 2, 100, 500 nm and fixed Pt thickness of 30 nm, periodically (every 1.5 h) measured at 0 V (versus RHE). Consistent with our hypothesis, the lifetime of metal-passivated GaAs photocathode increased with metal layer thickness because of the delayed proton transport.

Unassisted solar water splitting with tandem electrodes

Tandem systems composed of two series-connected GaAs electrodes (that is, a photocathode and photoanode) can supply a sufficient photovoltage to drive water splitting with sunlight as the only energy input $^{11,12,40-42}$. To demonstrate this concept using the high-performance bifacial III–V electrode design, we also fabricated GaAs photoanodes for water oxidation based on 'n-on-p' type epitaxial stacks (Supplementary Fig. 3), following the same fabrication steps for photocathodes (Fig. 1a). As a co-catalyst for the oxygen evolution reaction (OER), nanoporous thin films ($t \sim 60\,\mathrm{nm}$) of hydrous iridium oxide (IrO $_x$ ·nH $_2$ O, Supplementary Fig. 12) were anodically deposited directly on the p-type ohmic contact (Pt/Ti/Pt/Au/Ti/Pt = 10 nm/40 nm/10 nm/150 nm/2 nm/30 nm) using previously reported procedures 43,44 . The independently prepared GaAs photocathode and photoanode were released from their respective growth wafers and then co-integrated side by side (distance between electrodes: \sim 4.3 mm, Supplementary Fig. 13)

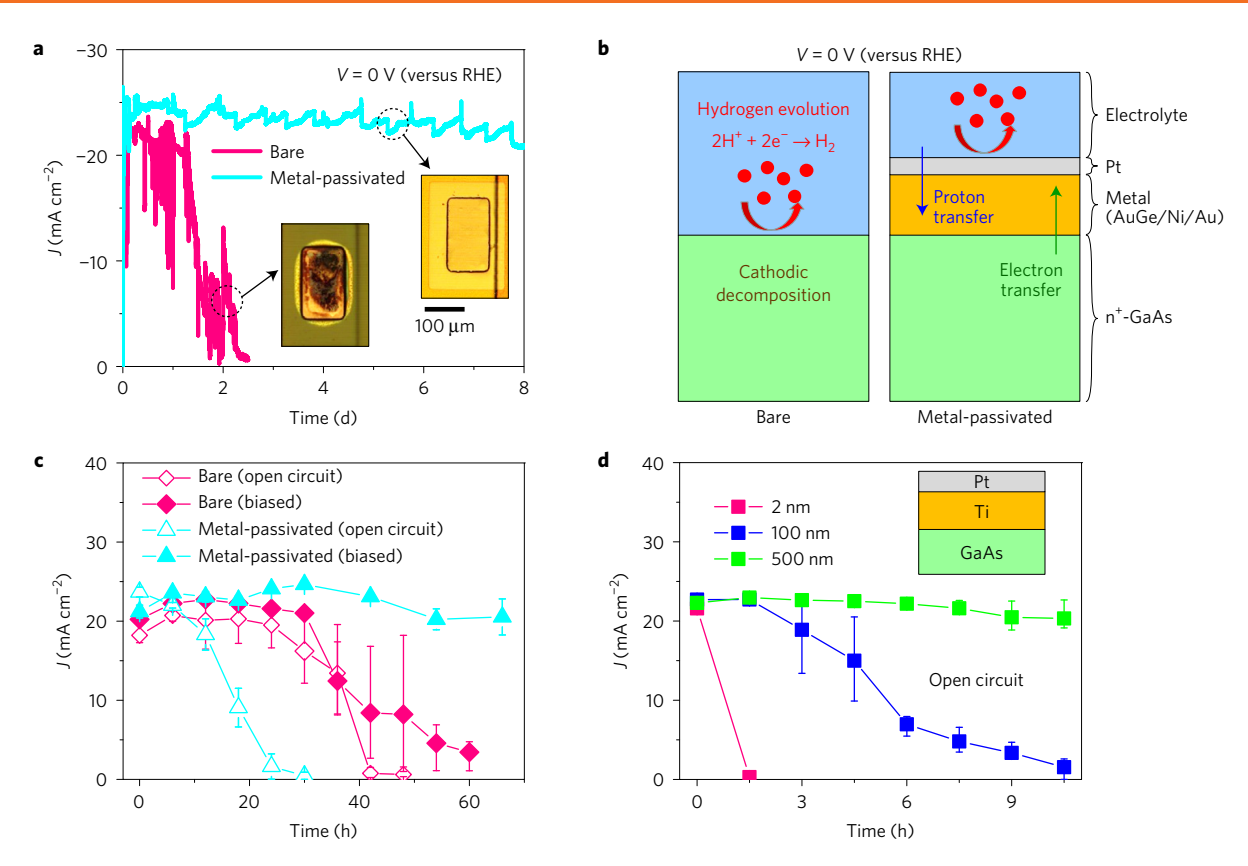


Figure 4 | Stability of integrated bifacial GaAs photocathodes. a, Current density-time (*J-t*) plots of integrated GaAs photocathodes in two different materials configurations at the catalytic interface, such as bare and metal-passivated (that is, an ohmic contact and Pt) GaAs in an acidic electrolyte (0.5 M H₂SO₄), measured under simulated AM 1.5G illumination at an applied potential of 0 V (versus RHE). The insets show optical micrographs of the surfaces of the respective electrodes taken during the measurement. **b**, Schematic illustration of bare and metal-passivated GaAs photocathodes and relevant photophysical and photoelectrochemical processes affecting the materials stability, including hydrogen evolution, cathodic decomposition of GaAs, electron transfer, and proton transfer. The red circles depict hydrogen bubbles generated from the photocathode. Directly exposed to the acidic electrolyte under cathodic conditions, the bare GaAs (left panel) is subject to the reductive decomposition. In the metal-passivated GaAs photocathode (right panel), on the other hand, metal layers serve as a diffusion barrier for protons, thereby effectively delaying the corrosion process. **c**, Current density of GaAs photocathodes under the same condition as in **a**, with (filled symbols) and without (that is, open circuit; open symbols) the applied bias (0 V versus RHE). Diamonds and triangles correspond to the bare and metal-passivated photocathodes, respectively. The unbiased electrode was immersed in the electrolyte without applying potential except during the measurement of the current. **d**, Current density of GaAs photocathodes deposited with bilayer metals at various Ti thicknesses. The electrode remained unbiased (that is, open circuit) except for the current measurement at 0 V (versus RHE) every 1.5 h. The inset illustrates the cross-sectional configuration of metal layers at the catalytic interface of GaAs photocathodes. Error bars in **c** and **d** represent the range of values obtained from three separate measure

on a single glass substrate to form the series-connected, wireless tandem photoelectrode system illustrated in Fig. 5a,b. It should be mentioned that the tandem electrode system presented here is mainly for demonstrating the capability of the integrated bifacial electrode design in unassisted water splitting with minimum degrees of system-level optimization, including the separation of product gases¹² or the use of earth-abundant co-catalysts^{45,46}.

The photovoltaic J-V curves of each individual electrode and the series-connected tandem system appear in Fig. 5c, where the short-circuit current density, open-circuit voltage and fill factor of the tandem system are $10.3\,\mathrm{mA\,cm^{-2}}$, $1.898\,\mathrm{V}$ and 0.80, respectively (Supplementary Table 2), measured under simulated AM1.5G solar illumination $(1,000\,\mathrm{W\,m^{-2}})$. To accurately evaluate the performance with a minimum contribution of waveguided photons, the illumination area was confined by using lithographically defined metal apertures ($\sim 750 \times 750\,\mathrm{\mu m^2}$, Supplementary Fig. 14). Figure 5d shows the individually measured J-E performance of the photocathode and photoanode in a three-electrode configuration under simulated one-sun illumination. A projected operating current density of the tandem system from the intersection of J-E curves was $\sim 10.3\,\mathrm{mA\,cm^{-2}}$, corresponding

to a solar-to-hydrogen efficiency ($\eta_{\rm STH}$) of \sim 12.7% assuming 100% Faradaic efficiency. The short-circuit current density of the integrated tandem photocathode/photoanode system was also measured directly in a two-electrode configuration, giving 10.6 mA cm⁻² and 13.1% solar-to-hydrogen efficiency (Fig. 5e and Supplementary Video 1), in good agreement with the graphically obtained value (Fig. 5d). In parallel to the J-E measurements, the amount of product gases generated from the tandem electrode system were separately monitored by a mass spectrometer to accurately evaluate $\eta_{\rm STH}$, where average Faradaic efficiencies of 98.2% with a standard deviation of 3.1% for H_2 and 104.0% with a standard deviation of 3.7% for O_2 were obtained with respect to the Pt wire electrode, thus confirming Faradaic efficiencies of unity and the negligible cross-diffusion of product gases within the precision of the measurement (Supplementary Table 3).

Conclusions

In summary, we demonstrated a materials platform for III–V compound semiconductor photoelectrodes that can overcome many limitations of conventional wafer-based solar water-splitting systems. Printed assemblies of epitaxially grown GaAs photoelectrodes

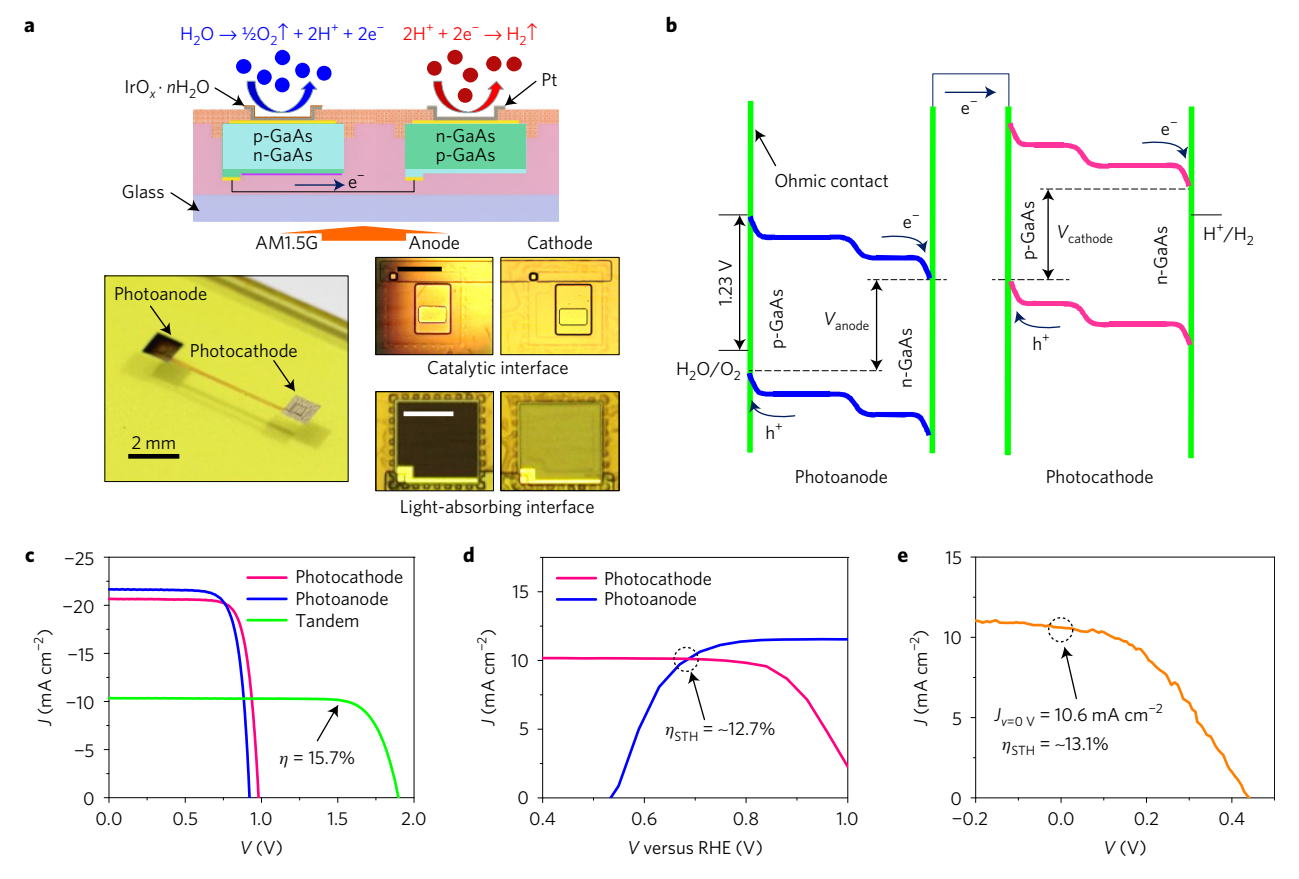


Figure 5 | Unassisted solar water splitting with a tandem electrode system of bifacial GaAs photoelectrodes. a, Schematic illustration (top), photographic image (bottom left), and optical micrographs (bottom right) of tandem electrode system for unassisted solar water splitting, where separately prepared GaAs photocathode and photoanode are co-integrated on a glass substrate. The length of the scale bars in the optical micrographs (bottom right) is $300 \,\mu\text{m}$. The red and blue circles in the illustration depict hydrogen and oxygen bubbles generated from the photocathode and photoanode, respectively. b, Corresponding energy band diagram of the tandem system. c, Representative J-V curves of GaAs photocathode, photoanode, and series-connected tandem system, measured under simulated AM1.5G solar illumination. Note that the J_{sc} of a photoanode is slightly higher than a photocathode due to the ARC. d, Representative J-E curves of printed GaAs photocathode (pink) and photoanode (blue) with an ohmic metal contact (photocathodes: AuGe/Ni/Au = $100 \, \text{nm}/30 \, \text{nm}/150 \, \text{nm}$, photoanodes: Pt/Ti/Pt/Au = $10 \, \text{nm}/40 \, \text{nm}/10 \, \text{nm}/150 \, \text{nm}$) and Pt ($30 \, \text{nm}$) in an acidic electrolyte ($30 \, \text{nm}$

provide a practical pathway to control and independently optimize light absorption, charge transfer, electrocatalysis, and corrosion resistance, while also realizing a significant reduction of the expensive materials cost. The integrated bifacial electrode design with decoupled optical and reactive interfaces enabled the implementation of optically opaque metal layers as an ohmic contact and HER co-catalyst, enhancing both charge transfer and corrosion resistance. This approach suppresses the cathodic decomposition of GaAs via thick metal layers that improve electron transfer and proton consumption while inhibiting proton diffusion, leading to the efficient and stable water reduction for eight days in strong acid. The integrated electrode platform with optically, electronically and electrochemically engineered configurations permitted a ~13.1% solar-to-hydrogen efficiency in an unassisted mode of solar-driven water splitting based on a wireless tandem system of GaAs photoelectrodes. The performance and cost-effectiveness of the reported tandem electrode can be further improved by implementing more advanced system designs, such as the separation of product gases and the use of earth-abundant co-catalysts.

We believe that the materials design and fabrication concepts presented in this study can be readily applied to a variety of materials (for example, group IV, III–V, III–N) and electrochemical reactions (for example, CO_2 or N_2 reduction). Such systems

could benefit from strategically tailored materials interfaces for photocatalysis, where greatly expanded and unconventional combinations of materials at the catalytic interface of semiconductor photoelectrodes could enable new paradigms in performance, stability and economics of solar fuel generation.

Methods

Fabrication of integrated bifacial GaAs photoelectrodes. Epitaxial materials of 'p-on-n' and 'n-on-p' type GaAs solar cells as photocathodes and photoanodes, respectively, were grown on a (100) semi-insulating GaAs wafer using metal organic chemical vapour deposition (MOCVD)^{28,47}. The fabrication of GaAs photocathodes using a p-on-n epitaxial stack started with the electron-beam evaporation (Temescal) and lift-off of a p-type ohmic metal contact (Pt/Ti/Pt/Au: 10 nm/40 nm/10 nm/80 nm), followed by the wet chemical etching of p+-GaAs using a mixture (4:1 by volume) of citric acid (C₆H₈O₇) and hydrogen peroxide $(H_2O_2)^{28}$, and the deposition of silicon nitride (Si_3N_4) on the exposed window layer as an ARC by plasma enhanced chemical vapour deposition (PECVD, Oxford PlasmaPro System 100). Microscale (\sim 500 \times 500 μ m²) electrode areas were delineated by photolithography (AZ5214, Merck KGaA) and wet chemical etching (phosphoric acid (H₃PO₄):deionized (DI) water:H₂O₂ = 1:12:13 and $C_6H_8O_7$: $H_2O_2 = 4:1$ by volume). Upon the undercut etching of the sacrificial layer (Al_{0.95}Ga_{0.05}As) in a diluted hydrochloric acid (HCl (38%, EMD):DI water = 1:4 by volume), arrays of GaAs photocathodes were released from the growth wafer and printed on a glass substrate by an elastomeric stamp made of polydimethylsiloxane (Silgard 184, Dow Corning) using photocurable polyurethane (NOA 61, Norland Products) as a printing medium. On the

exposed n*-GaAs, an n-type metal contact (AuGe/Ni/Au: 100 nm/30 nm/150 nm) was then deposited by electron-beam evaporation, followed by wet chemical etching (H $_3$ PO $_4$:DI water:H $_2$ O $_2$ = 1:12:13) to expose the p-type metal contact and form metal interconnects. A thin ($\sim\!4\,\mu m$) layer of polyimide (PI2525, HD Microsystems) was spin-coated and cured (250 °C, 60 min) under a N $_2$ atmosphere. Subsequently, the PI in the central region of the electrode was etched by oxygen reactive ion etching (100 W, 100 mtorr, 15 min) to define the active electrode surface. Connecting readout electrical wires to the printed photocathodes using flexible anisotropic conductive film (ACF, Elform) completes the fabrication process of the GaAs photocathodes. Fabrication of GaAs photoanodes using 'n-on-p' epitaxial stack followed the same procedure with switched sequences of metal deposition. Complete details of the fabrication steps are available in Supplementary Information.

Deposition of iridium oxide OER catalysts. As a catalyst for the oxygen evolution reaction (OER), nanoporous thin films ($t \sim 60 \, \mathrm{nm}$) of hydrous iridium oxide (IrO $_x$ · nH $_2$ O) were formed on the metal (that is, Pt) layer of the printed GaAs photoanodes through an anodic electrodeposition process^{43,44}. The monomeric precursors ([Ir(OH) $_6$) 2 -]) were prepared by heating a solution of K $_2$ IrCl $_6$ (2 mM in 0.04 wt% aqueous NaOH) to 70 °C, followed by rapid cooling in an ice bath. The anodic deposition on the GaAs photoanode was then conducted in 0.2 mM [Ir(OH) $_6$) 2 -] solution at an applied potential of 1 V versus Ag/AgCl for 20 min in a three-electrode configuration with a Pt pad as a counter electrode.

Reflectance and PV measurements. Reflectance spectra of GaAs photoelectrodes were recorded using a home-made optical set-up consisting of a white light source (HL-2000, Ocean Optics) and a fibre-optic spectrometer (Flame-T-VIS-NIR, Ocean Optics). The source light was collimated by an achromatic doublet lens ($f=19\,\mathrm{mm}$, N.A. = 0.42) and then focused on the cell region (beam diameter =~ 50 $\mu\mathrm{m}$) through an objective lens (20×, N.A. = 0.4). The reflected light was collected by the same objective lens and guided to the spectrometer through a multimode fibre. A silver mirror deposited on fused silica (PF10-03-P01, Thorlabs) was used as a 100% calibration standard. The photovoltaic performance was characterized using a semiconductor parameter analyser (4156C, Agilent) and a full spectrum solar simulator (94042A, Oriel), where the illumination intensity of one sun (~1,000 W m $^{-2}$) was calibrated using a reference silicon solar cell (91150V, Newport).

PEC measurements. All PEC measurements in a three-electrode configuration were performed in an aqueous solution (0.5 M, pH = 0.55) of sulfuric acid (H₂SO₄, EMD Chemicals, ACS grade, 95–98%) under simulated AM 1.5G solar illumination (1,000 W m⁻²). Linear sweep voltammetry data were collected by a potentiostat (Reference 600, Gamry) under a three-electrode configuration with Ag/AgCl (RE-5B, Bioanalytical Systems, 3M KCl, 0.206 V versus NHE) and platinum (MW-1032, Bioanalytical Systems) as reference and counter electrodes, respectively, where the potential of the working electrode was scanned from -0.8 to 1.1 V (versus RHE) for photocathodes (from 1.2 V to -0.3 V (versus RHE) for photoanodes) at a scan rate of 200 mV s $^{-1}$. For the conversion of electrode potential from Ag/AgCl to the reversible hydrogen electrode (RHE), a linear voltammetry scan was performed using a platinum electrode (MF-2013, Bioanalytical Systems) as a cathode to determine the onset potential of hydrogen production. For chronoamperometry measurements, the potential of the working electrode was maintained at 0 V (versus RHE) during the current measurement.

One-sun benchmarking measurements for a tandem electrode system in a two-electrode configuration were performed at the Solar Radiation Research Laboratory (SRRL) at the National Renewable Energy Laboratory (NREL). Direct solar irradiance was measured every minute by a pyrheliometer (Kipp & Zonen), and spectral data were collected ever five minutes by a spectroradiometer (Prede PGS-100). The device benchmarked was illuminated through a 5° field-of-view collimating tube (ASTM E1125-99). Spectral correction was performed using IPCE and real-time spectral data following established procedures based on those used for primary reference cell calibration 48,49 . The potentiostat lead for the working electrode was attached to the photocathode, and the leads for the counter and reference electrodes were connected together to the photoanode of the tandem system. The potential of the working electrode was scanned from -0.4 to $1.0\,\mathrm{V}$ at a scan rate of $20\,\mathrm{mV}\,\mathrm{s}^{-1}$. Electrochemical impedance spectroscopy (EIS) measurements of GaAs photocathodes were performed in a three-electrode configuration under AM 1.5G illumination at 0.3 V (versus RHE), where the sinusoidal perturbation of potential was 10 mV and the frequency range was between 10 Hz to 100 MHz.

FE measurements. For Faradaic efficiency (FE) measurements, the tandem electrode for unassisted water splitting was mounted on a 10-ml PEC cell using a silicone adhesive (RTV 118, Momentive), where 8 ml of $0.5\,\mathrm{M}$ $\mathrm{H}_2\mathrm{SO}_4$ was continuously sparged with ultrahigh-purity Ar maintained at 1.5 standard cubic centimetres per minute (sccm) by a mass flow controller. The outlet Ar flow was sampled at intervals of 1 s with a capillary quadrupole mass spectrometer

(ThermoStar GSD320, Pfeiffer). The mass spectrometer response (that is, ion current) for H₂ and O₂ was measured in amperes with a Faraday cup type detector, where N2 and Ar were also monitored for leak detection. The mass-to-charge ratios (m/z) monitored were 2, 32, 28 and 40 for H_2 , O_2 , N_2 and Ar, respectively, using a sampling time of 200 ms for each species. Before each calibration or sample measurement, Ar was bubbled through the cell for approximately 20-30 min to purge the electrolyte but also establish stable H₂ and O₂ baseline signals. Calibration was performed via electrolysis using Pt electrodes (99.997%, Premion) by passing a fixed amount of total charge at a constant current (that is, 0.060 C by passing 100 µA for 10 min), where the ion current from mass spectrometer for H2 and O2 were integrated after fitting and subtracting a linear baseline. The sample measurement was performed at short-circuit under a tungsten lamp intensity set to target 100 μA constant photocurrent (about two suns). After a cumulative 0.060 C were passed, the sample was returned to dark, open-circuit conditions. Five calibration measurements and three sample measurements were performed, obtaining average Faradaic yields of 98.2% with a standard deviation of 3.1% for H₂ and 104.0% with a standard deviation of 3.7% for O2, thus confirming Faradaic efficiencies of unity within the precision of the measurement.

IPCE measurements. IPCE measurements were performed in a three-electrode configuration using a mercury/mercurous sulfate reference electrode (MSE) in an aqueous solution (0.5 M) of sulfuric acid (5100A, Koslow Scientific). A 300 W xenon arc lamp (67005, Newport) and monochromator (SP-50, Acton) provided monochromatic illumination in 10-nm increments having <10 nm full-width at half-maximum⁴⁹. Overfill illumination was used, where the flux density was measured at each wavelength using a calibrated Si photodiode (S1336-8BQ, Hamamatsu). The illumination was chopped once at each wavelength at a frequency of 0.2 Hz, sufficiently slow to avoid transient capacitive current, and the final one second of data in each illuminated cycle was averaged and dark current subtracted to obtain the photocurrent at each wavelength.

Optical modelling. Reflectance and absorption spectra of GaAs photoelectrodes on a growth wafer and a glass substrate were numerically modelled by a finite-difference time-domain method (FDTD, Lumerical Solutions) 32,33 . For calculations at normal incidence, a three-dimensional simulation volume was defined with periodic boundary conditions for the x- and y-directions, and a perfectly matched layers (PML) boundary condition for the z-direction, where a continuous plane wave that has a broad Gaussian frequency spectrum $(270-750 \, \text{THz or } 400-1,100 \, \text{nm})$ was assumed as a light source. To simulate reflectance spectra of Pt-deposited GaAs photoelectrodes, a three-dimensional image of the Pt film reconstructed based on a top-view SEM image using software (Rhinoceros) was imported to the FDTD program, where the areal coverage of Pt was adjusted to match with the measured reflectance spectra.

Data availability. The data that support the plots within this paper and other findings of this study are available from the corresponding author upon reasonable request.

Received 9 September 2016; accepted 22 February 2017; published 27 March 2017

References

- Powell, D. M. et al. Crystalline silicon photovoltaics: a cost analysis framework for determining technology pathways to reach baseload electricity costs. Energy Environ. Sci. 5, 5874–5883 (2012).
- Kang, M. H. & Rohatgi, A. Quantitative analysis of the levelized cost of electricity of commercial scale photovoltaics systems in the US. Sol. Energy Mater. Sol. Cells 154, 71–77 (2016).
- Cook, T. R. et al. Solar energy supply and storage for the legacy and nonlegacy worlds. Chem. Rev. 110, 6474–6502 (2010).
- Lewis, N. S. & Nocera, D. G. Powering the planet: chemical challenges in solar energy utilization. *Proc. Natl Acad. Sci. USA* 103, 15729–15735 (2006).
- Fujishima, A. & Honda, K. Electrochemical photolysis of water at a semiconductor electrode. *Nature* 238, 37–38 (1972).
- Walter, M. G. et al. Solar water splitting cells. Chem. Rev. 110, 6446–6473 (2010).
- Lin, F. D. & Boettcher, S. W. Adaptive semiconductor/electrocatalyst junctions in water-splitting photoanodes. *Nat. Mater.* 13, 81–86 (2014).
- Kim, D., Sakimoto, K. K., Hong, D. C. & Yang, P. D. Artificial photosynthesis for sustainable fuel and chemical production. *Angew Chem. Int. Ed.* 54, 3259–3266 (2015).
- Lee, M. H. et al. p-Type InP nanopillar photocathodes for efficient solar-driven hydrogen production. Angew Chem. Int. Ed. 51, 10760–10764 (2012).
- 10. Gu, J. et al. Water reduction by a p-GaInP2 photoelectrode stabilized by an amorphous ${\rm TiO_2}$ coating and a molecular cobalt catalyst. Nat. Mater. 15, 456–460 (2016).

- Khaselev, O. & Turner, J. A. A monolithic photovoltaic-photoelectrochemical device for hydrogen production via water splitting. *Science* 280, 425–427 (1998).
- 12. Verlage, E. et al. A monolithically integrated, intrinsically safe, 10% efficient, solar-driven water-splitting system based on active, stable earth-abundant electrocatalysts in conjunction with tandem III–V light absorbers protected by amorphous TiO₂ films. Energy Environ. Sci. 8, 3166–3172 (2015).
- Pinaud, B. A. et al. Technical and economic feasibility of centralized facilities for solar hydrogen production via photocatalysis and photoelectrochemistry. Energy Environ. Sci. 6, 1983–2002 (2013).
- Dumortier, M. & Haussener, S. Design guidelines for concentrated photo-electrochemical water splitting devices based on energy and greenhouse gas yield ratios. *Energy Environ. Sci.* 8, 3069–3082 (2015).
- Woodhouse, M. & Goodrich, A. A Manufacturing Cost Analysis Relevant to Single- and Dual-Junction Photovoltaic Cells Fabricated with III-Vs and III-Vs Grown on Czochralski Silicon NREL Report PR-6A20-60126, 92 (NREL, 2014).
- Erne, B. H., Stchakovsky, M., Ozanam, F. & Chazalviel, J. N. Surface composition of n-GaAs cathodes during hydrogen evolution characterized by in situ ultraviolet-visible ellipsometry and in situ infrared spectroscopy. J. Electrochem. Soc. 145, 447–456 (1998).
- Ostermayer, F. W. & Kohl, P. A. Photoelectrochemical etching of p-GaAs. Appl. Phys. Lett. 39, 76–78 (1981).
- Hu, S. et al. Amorphous TiO₂ coatings stabilize Si, GaAs, and GaP photoanodes for efficient water oxidation. Science 344, 1005–1009 (2014).
- Scheuermann, A. G. et al. Design principles for maximizing photovoltage in metal-oxide-protected water-splitting photoanodes. Nat. Mater. 15, 99–105 (2016).
- Chen, Y. W. et al. Atomic layer-deposited tunnel oxide stabilizes silicon photoanodes for water oxidation. Nat. Mater. 10, 539–544 (2011).
- 21. Kenney, M. J. et al. High-performance silicon photoanodes passivated with ultrathin nickel films for water oxidation. Science 342, 836–840 (2013).
- Ji, L. et al. A silicon-based photocathode for water reduction with an epitaxial SrTiO₃ protection layer and a nanostructured catalyst. Nat. Nanotech. 10, 84–90 (2015).
- 23. Sun, K. et al. Nickel oxide functionalized silicon for efficient photo-oxidation of water. Energy Environ. Sci. 5, 7872–7877 (2012).
- Fan, F. R. F., Keil, R. G. & Bard, A. J. Semiconductor electrodes. 48.
 Photo-oxidation of halides and water on N-silicon protected with silicide layers. J. Am. Chem. Soc. 105, 220–224 (1983).
- Lin, Y. et al. Amorphous Si thin film based photocathodes with high photovoltage for efficient hydrogen production. Nano Lett. 13, 5615–5618 (2013).
- Nielander, A. C., Shaner, M. R., Papadantonakis, K. M., Francis, S. A. & Lewis, N. S. A taxonomy for solar fuels generators. *Energy Environ. Sci.* 8, 16–25 (2015).
- 27. Yablonovitch, E., Gmitter, T., Harbison, J. P. & Bhat, R. Extreme selectivity in the lift-off of epitaxial GaAs films. *Appl. Phys. Lett.* **51**, 2222–2224 (1987).
- Yoon, J. et al. GaAs photovoltaics and optoelectronics using releasable multilayer epitaxial assemblies. Nature 465, 329–333 (2010).
- Cheng, C. W. et al. Epitaxial lift-off process for gallium arsenide substrate reuse and flexible electronics. Nat. Commun. 4, 1577 (2013).
- Kang, D., Lee, S. M., Kwong, A. & Yoon, J. Dramatically enhanced performance of flexible micro-VCSELs via thermally engineered heterogeneous composite assemblies. Adv. Opt. Mater. 3, 1072–1078 (2015).
- Yoon, J. et al. Flexible concentrator photovoltaics based on microscale silicon solar cells embedded in luminescent waveguides. Nat. Commun. 2, 343 (2011).
- Lee, S. M. et al. Printable nanostructured silicon solar cells for high-performance, large-area flexible photovoltaics. ACS Nano 8, 10507–10516 (2014).
- Lee, S. M. et al. High performance ultrathin GaAs solar cells enabled with heterogeneously integrated dielectric periodic nanostructures. ACS Nano 9, 10356–10365 (2015).
- Bhatt, M. D. & Lee, J. S. Recent theoretical progress in the development of photoanode materials for solar water splitting photoelectrochemical cells. J. Mater. Chem. A 3, 10632–10659 (2015).
- Shen, L. et al. Nanostructured silicon photocathodes for solar water splitting patterned by the self-assembly of lamellar block copolymers. ACS Appl. Mater. Interfaces 7, 26043–26049 (2015).

- Dimroth, F. et al. Wafer bonded four-junction GaInP/GaAs//GaInAsP/GaInAs concentrator solar cells with 44.7% efficiency. Prog. Photovolt. 22, 277–282 (2014)
- King, R. R. et al. 40% efficient metamorphic GaInP/GaInAs/Ge multijunction solar cells. Appl. Phys. Lett. 90, 183516 (2007).
- Park, S. M. & Barber, M. E. Thermodynamic stabilities of semiconductor electrodes. J. Electroanal. Chem. 99, 67–75 (1979).
- Hagio, M. Electrode-reaction of GaAs metal-semiconductor field-effect transistors in deionized water. J. Electrochem. Soc. 140, 2402–2405 (1993).
- Coridan, R. H. et al. Methods for comparing the performance of energy-conversion systems for use in solar fuels and solar electricity generation. Energy Environ. Sci. 8, 2886–2901 (2015).
- Abdi, F. F. et al. Efficient solar water splitting by enhanced charge separation in a bismuth vanadate-silicon tandem photoelectrode. Nat. Commun. 4, 2195 (2013).
- 42. Jacobsson, T. J., Fjallstrom, V., Sahlberg, M., Edoff, M. & Edvinsson, T. A monolithic device for solar water splitting based on series interconnected thin film absorbers reaching over 10% solar-to-hydrogen efficiency. *Energy Environ. Sci.* 6, 3676–3683 (2013).
- Zhao, Y. X., Hernandez-Pagan, E. A., Vargas-Barbosa, N. M., Dysart, J. L. & Mallouk, T. E. A high yield synthesis of ligand-free iridium oxide nanoparticles with high electrocatalytic activity. *J. Phys. Chem. Lett.* 2, 402–406 (2011).
- 44. Zhao, Y. X., Vargas-Barbosa, N. M., Hernandez-Pagan, E. A. & Mallouk, T. E. Anodic deposition of colloidal iridium oxide thin films from hexahydroxyiridate(IV) solutions. *Small* 7, 2087–2093 (2011).
- Brown, D. E., Mahmood, M. N., Turner, A. K., Hall, S. M. & Fogarty, P. O. Low overvoltage electrocatalysts for hydrogen evolving electrodes. *Int. J. Hydrog. Energy* 7, 405–410 (1982).
- Landon, J. et al. Spectroscopic characterization of mixed Fe-Ni oxide electrocatalysts for the oxygen evolution reaction in alkaline electrolytes. ACS Catal. 2, 1793–1801 (2012).
- Kang, D. S. *et al.* Carbon-doped GaAs single junction solar microcells grown in multilayer epitaxial assemblies. *Appl. Phys. Lett.* 102, 253902, (2013).
- Osterwald, C. R. Translation of device performance-measurements to reference conditions. Sol. Cells 18, 269–279 (1986).
- Doscher, H., Young, J. L., Geisz, J. F., Turner, J. A. & Deutsch, T. G. Solar-to-hydrogen efficiency: shining light on photoelectrochemical device performance. *Energy Environ. Sci.* 9, 74–80 (2016).

Acknowledgements

D.K., H.L., H.C., Y.X., B.G. and J.Y. gratefully acknowledge National Science Foundation (ECCS-1202522, ECCS-1509897), USC startup fund, and Hanwha Advanced Materials Non-tenured faculty award. T.G.D., J.L.Y. and W.E.K. acknowledge support by the US Department of Energy (DOE), Office of Energy Efficiency & Renewable Energy, Fuel Cell Technologies Office under Contract No. DE-AC36-08GO28308 with the National Renewable Energy Laboratory. The authors thank D. Zhu and J. Curulli for help using facilities at Keck Photonics Laboratory and Center for Electron Microscope and MicroAnalysis (CEMMA) at USC, respectively.

Author contributions

J.Y. and D.K. conceived the idea and designed the experiment. D.K., J.L.Y., H.L., W.E.K., H.C., Y.X., B.G., T.G.D. and J.Y. performed the experiments. D.K., J.L.Y., H.L., W.E.K., H.C., T.G.D. and J.Y. analysed the data. D.K., J.L.Y., W.E.K., T.G.D. and J.Y. wrote the paper.

Additional information

Supplementary information is available for this paper.

Reprints and permissions information is available at www.nature.com/reprints.

Correspondence and requests for materials should be addressed to J.Y.

How to cite this article: Kang, D. *et al.* Printed assemblies of GaAs photoelectrodes with decoupled optical and reactive interfaces for unassisted solar water splitting. *Nat. Energy* **2**, 17043 (2017).

Publisher's note: Springer Nature remains neutral with regard to jurisdictional claims in published maps and institutional affiliations.

Competing interests

The authors declare no competing financial interests.